International Journal of Fatigue 208 (2026) 109552

Contents lists available at ScienceDirect

International Journal of Fatigue

journal homepage: www.elsevier.com/locate/ijfatigue

Thermomechanical fatigue performance of additively manufactured Inconel 939

Ivo Šulák [a], Markéta Gálíková [a,b], Tomáš Babinský [a,c], Ladislav Poczklán [a], Ivo Kuběna [a,*], Stefan Guth [d]

[a] Institute of Physics of Materials, Czech Academy of Sciences, Žižkova 22, 616 00 Brno, Czech Republic
[b] CEITEC - Central European Institute of Technology, Brno University of Technology, 62100 Brno, Czech Republic
[c] PSI Center for Nuclear Engineering and Sciences, 5232 Villigen PSI, Switzerland
[d] Institute for Applied Materials, Karlsruhe Institute of Technology, Engelbert-Arnold-Strasse 4, D-76128 Karlsruhe, Germany

ARTICLE INFO

Keywords:
Nickel-based superalloy
Laser powder bed fusion
High-temperature fatigue
Deformation mechanisms
Persistent slip bands
Intergranular damage
Microtwinning

ABSTRACT

Additively manufactured nickel-based superalloy Inconel 939 (IN939) was subjected to in-phase and out-of-phase thermomechanical fatigue loading in the temperature range of 400–800 °C. Horizontally and vertically built cylindrical specimens were subjected to a three-step heat treatment and subsequently tested with mechanical strain amplitudes in the range of 0.3–0.9%. A constant heating and cooling rate of 10 °C/s was utilised, making the cycle period 80 s. Representative hysteresis loops, fatigue hardening/softening curves, cyclic stress–strain curves, and fatigue life curves are reported. The results show that, regardless of the load cycle, the horizontally built IN939 exhibits lower lifetimes than the vertically built alloy. This stems from a distinctive ⟨001⟩ texture in the building direction, which influences the stress response of the material. Higher stress amplitude values observed for horizontally built material contribute to faster fatigue crack initiation and propagation. The SEM observation revealed that, regardless of the building direction, the damage is mainly intergranular for in-phase loading and mixed for out-of-phase loading. Plastic strain localisation into persistent slip markings and formation of nanotwins was typical for out-of-phase loading. In contrast, dense dislocation networks and stacking fault formation within γ́ precipitates were observed for in-phase loading.

1. Introduction

Nickel-based superalloys underpin the hot sections of modern gas turbines, where components experience steep thermal gradients, cyclic transition loadings during start-up and shutdown, and sustained exposures to high temperatures during steady-state operation. Among these alloys, Inconel 939 (IN939) is a γ́–strengthened superalloy engineered for high temperature strength and oxidation/corrosion resistance that has recently attracted scientific attention as it is available for additive manufacturing (AM) [1–10]. AM offers clear benefits for IN939 components like shorter supply chains, possible lattice structures and internal–cooling features, and weight-efficient designs. Yet, it brings well-known process–structure pitfalls for high γ́ superalloys, including hot cracking, residual stresses, and defect populations [11–13]. AM also imparts a hierarchical, highly anisotropic microstructure: columnar grains are aligned with the build thermal gradient, strong textures (often ⟨001⟩ orientation), melt pool bands with interdendritic segregation, and as-built roughness that acts as stress concentrators [5,14,15].

Until recently, IN939 was considered unsuitable for AM due to its relatively high Ti and Al content [12]. However, after optimising printing parameters, it became possible to manufacture almost defect-free material [13]. Process-mapping studies have shown that IN939 can be fabricated with relative densities greater than 99.5% while enabling microstructural control (e.g., weak-texture equiaxed vs. ⟨001⟩ columnar grains) when using a pulsed-wave laser regime and carefully selected hatch spacing and scan speeds [4]. Complementary approaches to suppress cracks and porosity include elevated base-plate preheating and tuning of volumetric energy density [16], as well as layer-wise remelting, which modifies the melt-pool geometry and can lower crack/porosity incidence when applied judiciously [7]. Composition–level design has emerged as a particularly powerful lever: guided by CALPHAD-based cracking metrics, targeted Si additions (~2–3 wt%) reduce the amount of low-melting inter–dendritic liquid (C/B/Zr–enriched) late in solidification and have produced crack-free IN939

---

* Corresponding author.
E-mail address: kubena@ipm.cz (I. Kuběna).

https://doi.org/10.1016/j.ijfatigue.2026.109552
Received 3 December 2025; Received in revised form 1 February 2026; Accepted 2 February 2026

using Powder Bed Fusion – Laser Beam/Metals (PBF-LB/M) [17]. Follow-up processing of Si-modified feedstock in a commercial PBF-LB/M system likewise demonstrated substantially lower crack density and increased strength (with some ductility penalty) [18]. Beyond solute tuning, ceramic–particle-assisted approaches (e.g., TiB_2-decorated powders) have been reported to widen the printability window and suppress cracking while maintaining a strength-ductility balance [19].

Despite rapid progress in printability and heat-treatment protocols for IN939 [3,5,8,10], the service-relevant thermomechanical fatigue (TMF) of PBF-LB/M IN939 has not been systematically mapped. Overall, the area of mechanical properties remains relatively unexplored, as most studies focus exclusively on static experiments [1,5,6,10,19]. Kanagarajah [1] was the first to test PBF-LB/M IN939 under strain-controlled fatigue at room temperature and 750 °C. Although only one sample was tested for each temperature, this study showed that as-built material has a considerably longer fatigue lifetime than heat-treated IN939. However, the duration of the fatigue tests was very short, and in the long term, the as-built condition may not be a suitable choice, especially in the case of high-temperature experiments, where phase transformations may occur, negatively affecting the plasticity of the material [5,8]. Only recently, Babinský [20] systematically compared room-temperature low-cycle fatigue (LCF) of cast IN939 with PBF-LB/M variants, while varying build orientation (vertical vs. horizontal) and post-processing (non-treated vs. precipitation-hardened). The results underscored the dominant roles of build orientation and ageing-induced $\acute{\gamma}$ strengthening in governing fatigue behaviour as horizontal aged PBF-LB/M specimens achieved the best stress-life performance. In contrast, vertical as-built specimens exhibited the greatest resistance to cyclic plastic straining. A short incremental-step method explicitly probed the effect of building direction (B.D.) on cumulative plastic deformation at 800 °C and 900 °C [21]. Specimens with B.D. parallel to the loading axis accumulated far more plastic strain, ~27% at 800 °C and ~ 46% at 900 °C, than specimens with B.D. perpendicular to the loading axis (~1% and ~ 9%). This anisotropic response is rationalised by a strong ⟨001⟩ fibre texture along the B.D., which affects the modulus of elasticity and the overall elastic–plastic behaviour of the IN939.

These pioneering fatigue studies provide comprehensive coverage of the isothermal low-cycle fatigue behaviour of PBF-LB/M IN939. However, more complex and service-relevant thermomechanical fatigue (TMF) that captures the combined damage from cyclic thermal fields and cyclic mechanical straining, and is often considered as more detrimental than isothermal LCF [22,23], is yet unexplored for AM IN939. In uniaxial, strain-controlled TMF, a material experiences prescribed courses of temperature and mechanical strain. Typically, two courses are defined. Namely, in-phase (TMF-IP) when the tensile strain peak coincides with the temperature peak, and out-of-phase (TMF-OP) when the tensile strain peak coincides with the temperature minimum [22,24–28]. A robust pattern across polycrystalline nickel-based superalloys is that TMF-IP tends to be more damaging than TMF-OP under otherwise similar conditions at service-relevant temperatures [24,27–30]. Reasoning can be attributed to several factors, including the maximum tensile strain/stress occurring at the maximum temperature, promoting time-dependent tensile deformation (creep), grain boundary sliding/cavitation, and oxygen-assisted damage during the tensile part of the cycle. By contrast, TMF-OP tends to be dominated by cyclic fatigue and oxidation effects, where oxides form at high temperature while the material is in compression and then crack under the subsequent low temperature tensile portion, often seeding surface-controlled crack initiation. That said, the relative severity can invert at low strain amplitudes or with dwell times [25,26,28,31]. In the case of additively manufactured metals, TMF behaviour can be strongly influenced by the build orientation, as TMF crack initiation and propagation can be highly sensitive to the alignment with the loading axis. Differences in crack growth mechanisms and slip transfer across layers mean that vertical and horizontal specimens can exhibit distinct cyclic plasticity, oxidation-assisted damage, and crack growth rates, with trends dependent on the cycle type (TMF-IP vs. TMF-OP) [27,32–35].

This work addresses the TMF behaviour of PBF-LB/M–processed IN939. Both vertically and horizontally built specimens were subjected to TMF loading in the temperature range of 400-800 °C. The work performed here aims to outline the dominant TMF damage mechanisms and frame how PBF-LB/M–unique microstructural features alter fatigue crack initiation, fatigue crack growth, and what the implications are for TMF lifetime.

2. Experimental section

2.1. Manufacturing of IN939 superalloy

Test coupons were produced on an EOS M290 system using a 400 W ytterbium fibre laser. The feedstock was commercially available, gas-atomised EOS NickelAlloy IN939 powder with an average particle size of 40 ± 15 μm; its chemistry is given in Table 1. Fabrication of cylinders with a length of 150 mm and a diameter of 13 mm was carried out by a private company Innomia a.s. in an argon atmosphere (99.9%) to prevent oxidation, employing both horizontal and vertical build directions to assess their influence on the TMF behaviour of IN939. The processing parameters were a 40-μm layer thickness, a 60-μm hatch spacing, and a scan speed of 1300 mm/s. A stripe scan strategy was used with a 67° hatch rotation between successive layers. The build plate made of 316 L steel was preheated to 180 °C. After printing, specimens were cut from the build plate. A three-step heat treatment consisting of solution annealing at 1175 °C for 45 min, followed by two-step precipitation hardening at 1000 °C for 6 h and 800 °C for 4 h, was applied directly to the as-printed samples. Heat treatment was performed in air. The relative density of the PBF-LB/M IN939 obtained on five independent specimens by Archimedes' method was approximately 99.67 ± 0.13%.

2.2. Thermomechanical fatigue loading

Solid cylindrical TMF test specimens (Fig. 1a) with a gauge length of $L_0 = 16$ mm and a diameter of $d_0 = 7$ mm were heat-treated and subsequently machined in the workshop of the Institute of Physics of Materials. TMF testing was performed on a computer-controlled servo-hydraulic machine, MTS 880, with a load capacity of ± 50 kN. A fully reversed push–pull loading ($R_\varepsilon = -1$) under a strain-controlled regime was applied. Strain was measured with an air-cooled extensometer (12 mm gauge length) fitted with 120 mm ceramic tips to protect the sensitive electronics from heat. TMF tests covered a 400–800 °C temperature range with constant heating/cooling at 10 $°C.s^{-1}$, resulting in an 80 s cycle over the full temperature excursion. The corresponding strain rates were $1.5 \times 10^{-4}\ s^{-1}$ at the lowest mechanical strain amplitude (3×10^{-3}) and $4.5 \times 10^{-4}\ s^{-1}$ at the highest mechanical strain amplitude (9×10^{-3}). Mechanical strain amplitudes were selected to fall within the lifetime range of approximately 10^2 to 10^4 cycles. Specimens were heated inductively using a high-frequency tube generator. Temperature was monitored by three K-type ribbon thermocouples, which were attached at the gauge centre and both ends (indicated by red dots in Fig. 1a). The thermocouples were secured with heat-resistant fabric to ensure good contact and to minimise airflow-induced fluctuations. The whole experimental setup is described elsewhere [36]. Two TMF phasing conditions were applied: TMF-IP and TMF-OP (Fig. 1b). All procedures followed the “Validated Code-of-Practice for Strain-Controlled Thermo-Mechanical Fatigue Testing” [37]. Before TMF testing, thermal hysteresis was measured, and the coefficient of thermal expansion was determined. The adequacy of thermal-strain compensation was then confirmed via a zero-force check in which the peak stress remained below 25 MPa. Prior to TMF testing, the Young's modulus was evaluated using a load of up to 3 kN at temperatures of 400 °C and 800 °C. The average values obtained for vertical B.D. are (167 ± 13) GPa and (130 ± 12) GPa. Whereas for horizontal B.D., the values are higher, reaching (206 ± 11) GPa and (163 ± 15) GPa, respectively. The number

Table 1
Chemical composition of IN939 in wt.% evaluated by EDX and GD-OES.

	C	Cr	Co	W	Nb	Ti	Al	Ta	Zr	Cu	Ni
Powder EOS IN939	0.14	18.9	19.3	2.1	1.1	3.4	2.0	1.4	0.09	0.16	Bal.
PBF-LB/MIN939	0.15	18.8	19.6	2.4	1.2	3.4	2.0	1.4	0.09	0.15	Bal.

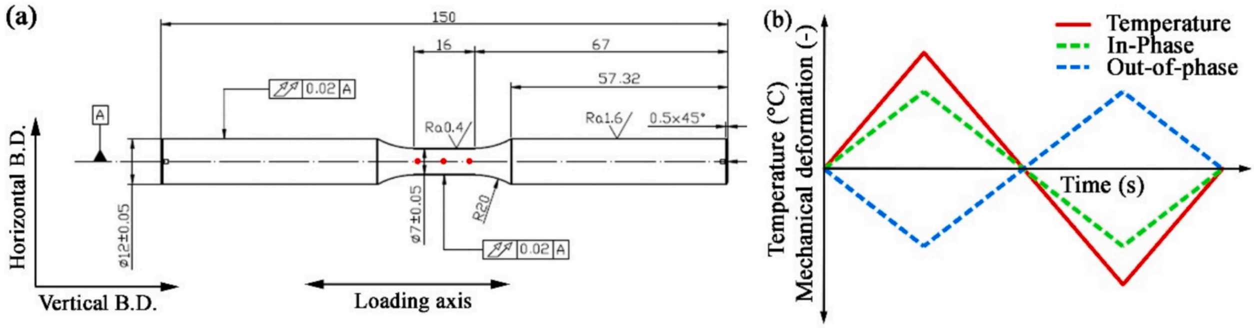

Fig. 1. (a) TMF specimen geometry with indicated B.D.; (b) TMF-IP and TMF-OP loading cycle.

of cycles to failure, Nf, for TMF cycling was defined as the number of elapsed cycles when the criterion given by equation (1) was met, or at the time of fracture if the criterion was not reached:

$$\frac{\left(\sigma^{i}_{max}-\sigma^{i}_{min}\right)-\sigma^{ref}_{a}}{\sigma^{ref}_{a}}\leq 0.7 \tag{1}$$

where σ^{i}_{max} and σ^{i}_{min} are maximum and minimum stress in *i*-cycle, and σ^{ref}_{a} is reference stress amplitude set at 10th cycle. The criterion is consistent with a fatigue crack extending through at least half the cross-section of the test specimen. The run-out was set to 10 000 cycles. All measuring equipment used was calibrated to ensure the validity of the data presented.

2.3. Observation techniques

Longitudinal sections of the gauge length before and after TMF testing were imaged using a scanning electron microscope (SEM) Tescan LYRA 3 XMU FEG-SEM/FIB fitted with an Oxford Instruments Symmetry 2 electron backscattered diffraction (EBSD) detector. SEM observation conditions were 10 kV for secondary-electron (SE) and backscattered electron (BSE) imaging and 20 kV for EBSD mapping. Both, SE and BSE imaging, and EBSD mapping were done on metallographic specimens prepared via standard grinding (SiC to P1200) followed by electro-polishing on a Struers LectroPol-5 using an electrolyte of 93.9 vol% ethanol, 1.4 vol% nitric acid, and 4.7 vol.% perchloric acid at − 12 °C and 30 V for 5–10 s. The chemical composition of both EOS IN939 powder and PBF-LB/M IN939 superalloy was analysed using an energy-dispersive X-ray (EDX) detector built into the SEM. Furthermore, glow discharge optical emission spectrometry (GD-OES) using GD-PROFILER 2 was used to measure light elements. Dislocation arrangement, cyclic plastic slip localisation, and γ' precipitates fraction were further characterised using a transmission electron microscope (TEM) Thermo Scientific Talos F200i operated at 200 kV in parallel-beam and convergent-beam modes. The Thermo Scientific Talos F200i is equipped with bright-field (BF) and high-angle annular dark-field (HAADF) detectors for observation in the scanning transmission (STEM) regime. Oriented TEM foils were prepared by standard electrolytic thinning: ~7 × 5 mm^2 plates (cut parallel to the loading axis) with an initial thickness of approximately 0.7 mm were ground to a thickness of 0.060 mm. Subsequently, discs with a 3 mm diameter were punched out of this plate in a manner that the loading axis can still be maintained, and after that, a double-jet thinning in a Struers TenuPol-2 with 70 vol% methanol, 20 vol% glycerin, and 10 vol.% perchloric acid at − 5 °C and 11 V was applied, producing ~ 80 nm-thick regions suitable for TEM scrutiny. The particle analysis was performed in ImageJ software, analysing over 1750 precipitates from 8 STEM images acquired with a magnification of 65kx.

3. Results

3.1. Initial microstructure of IN939 superalloy

The microstructure of the unloaded material is shown in Fig. 2. Examination by EBSD mapping confirmed elongated grains oriented along the B.D. with a predominant ⟨001⟩ crystallographic orientation parallel to the B.D. (Fig. 2b). The multiple uniform density (MUD) in the ⟨001⟩ direction was determined to be 5.2 ± 0.5, signifying a pronounced crystallographic texture parallel to the B.D. Perpendicular to the B.D., the preferred orientation is in the ⟨011⟩ direction with MUD around 3.4 ± 0.3 (Fig. 2a). The mean grain size, estimated from cuts parallel and perpendicular to the B.D., was 134.3 ± 93.1 and 14.8 ± 13.3 μm, respectively. The aspect ratio of the elongated grains, defined as the ratio of grain length to width in projections parallel and perpendicular to the B.D., was found to range between 4.3 and 9.1. The PBF-LB/M IN939 superalloy was almost defect-free. However, isolated defects such as gas porosity or lack of fusion could be observed in the structure (Fig. 2c). Grain boundaries (Fig. 2c) and dislocation-rich walls (Fig. 2e) are decorated with a fine dispersion of carbides enriched in Ta, Ti, and Nb. A three-step heat treatment, including solutioning and two-step ageing, led to a complex microstructure with a bimodal distribution of strengthening γ' precipitates, with a γ' fraction of 41.2 ± 5.8%. Coherent face-centred cubic γ' precipitates are homogenously distributed within the γ solid solution matrix (Fig. 2d). The size of fine and coarse γ' precipitates was determined to be 16.3 ± 4.4 nm and 159.4 ± 34.8 nm, respectively. Both types of γ' precipitates are spherical in shape, as shown in Fig. 2f. As can be seen from the SEM and TEM images, the heat treatment did not lead to the formation of undesirable brittle phases, nor did it cause recrystallisation or dissolve the cellular structure typical of PBF-LB/M processes. Particularly, remnants of the cellular structure may contribute to higher material strength, as dislocation walls can form additional barriers to the movement of mobile dislocations mediating plastic deformation.

3.2. Stress–strain response

The representative stress–strain hysteresis loops corresponding to the 1st, 10th, and $N_f/2$ cycle for the TMF tests conducted at a mechanical

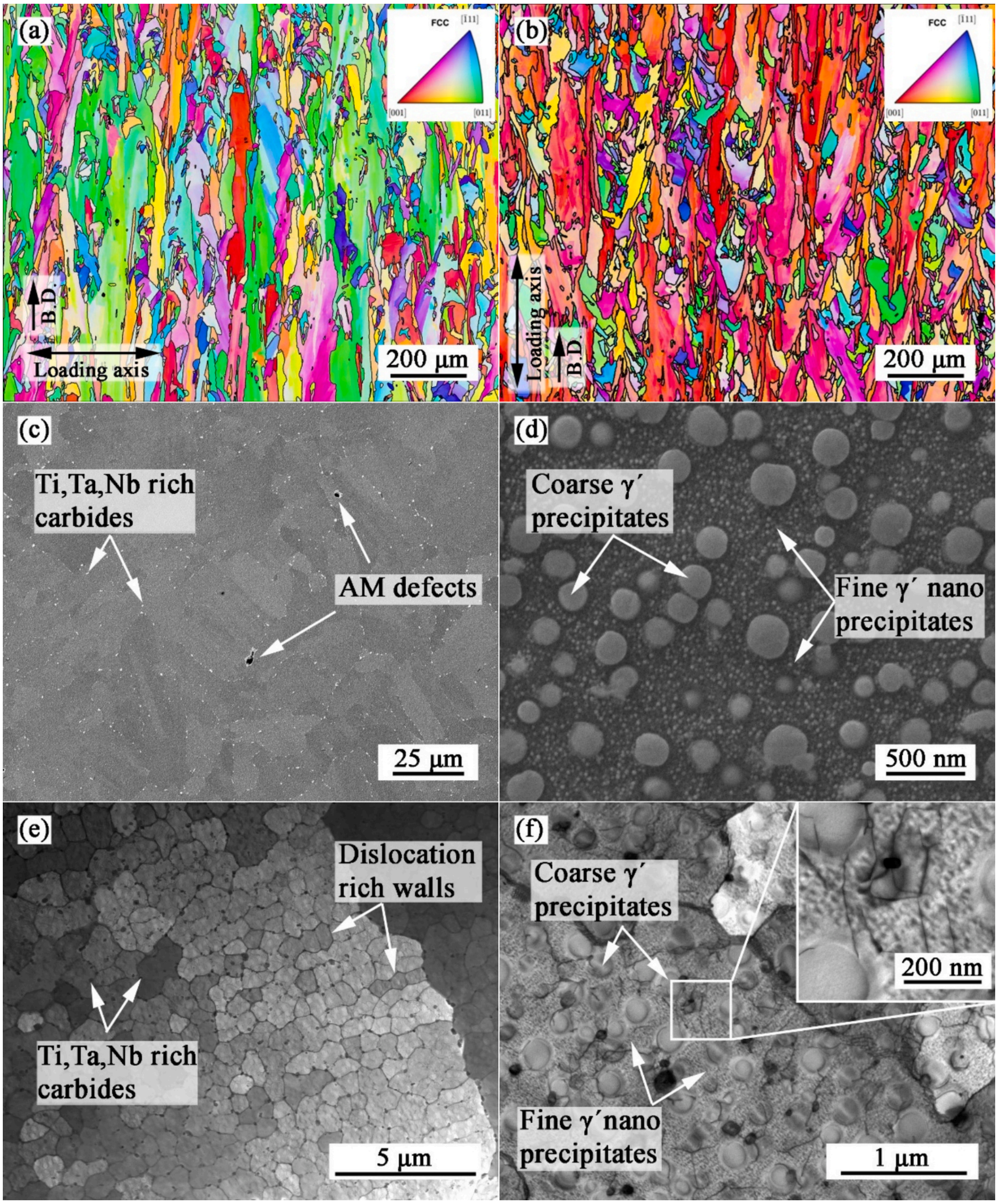

Fig. 2. Unloaded microstructure of PBF-LB/M IN939. (a) EBSD-IPFY map of horizontally built sample; (b) EBSD-IPFX map of vertically built sample; (c) SEM-BSE overview image of the microstructure showing occasional spherical AM defects; (d) SEM-SE image showing a bimodal distribution of $\acute{\gamma}$ precipitates; (e) STEM overview showing dislocation-rich cell structures; (f) STEM detail of $\acute{\gamma}$ precipitates.

strain amplitude of 5×10^{-3} are presented in Fig. 3. The distinct loop shapes arise from the cyclic variation of temperature within each loading cycle, which influences the stress response during strain-controlled loading. Variations in the shape and position of the hysteresis loops among the tests are directly associated with the imposed phase relationship between mechanical strain and temperature [28–30]. This is most evident in the development of mean stress, which is significantly compressive for TMF-IP loading. In contrast, substantial tensile mean stress is typical for TMF-OP loading. In the TMF-IP test performed at $\varepsilon_{\mathrm{amech}} = 5 \times 10^{-3}$ (Fig. 3a and Fig. 3c), the maximum tensile strain coincided with the peak temperature, whereas compressive strain occurred at the minimum temperature during each cycle. Considering the horizontally built IN939, the stress amplitude decreased from 767 MPa during the first cycle to 754 MPa at mid-life, indicating mild cyclic softening. For the vertically built superalloy, the stress amplitude dropped from 617 MPa to 584 MPa, demonstrating that preferential orientation in relation to the loading axis plays a significant role in the stress response. In contrast, for the TMF-OP test at the same strain amplitude (Fig. 3b and Fig. 3d), the peak temperature coincided with compressive loading, while the lowest temperature corresponded to the maximum tensile stress. In this case, the stress amplitude dropped from 767 MPa in the first loading cycle to 734 MPa at mid-life, for the horizontally built material, and from 668 MPa to 630 MPa for the vertically built IN939 superalloy. Saturated stress amplitudes at mid-life, together with plastic strain amplitude and number of cycles to failure for all performed tests, are listed in Table 2.

The cyclic stress response obtained from the TMF tests is presented in Fig. 4, where the maximal and minimal stresses are plotted as a function of the number of elapsed cycles. Fig. 4a and Fig. 4b represent the stress evolution of horizontally built specimens with the loading axis

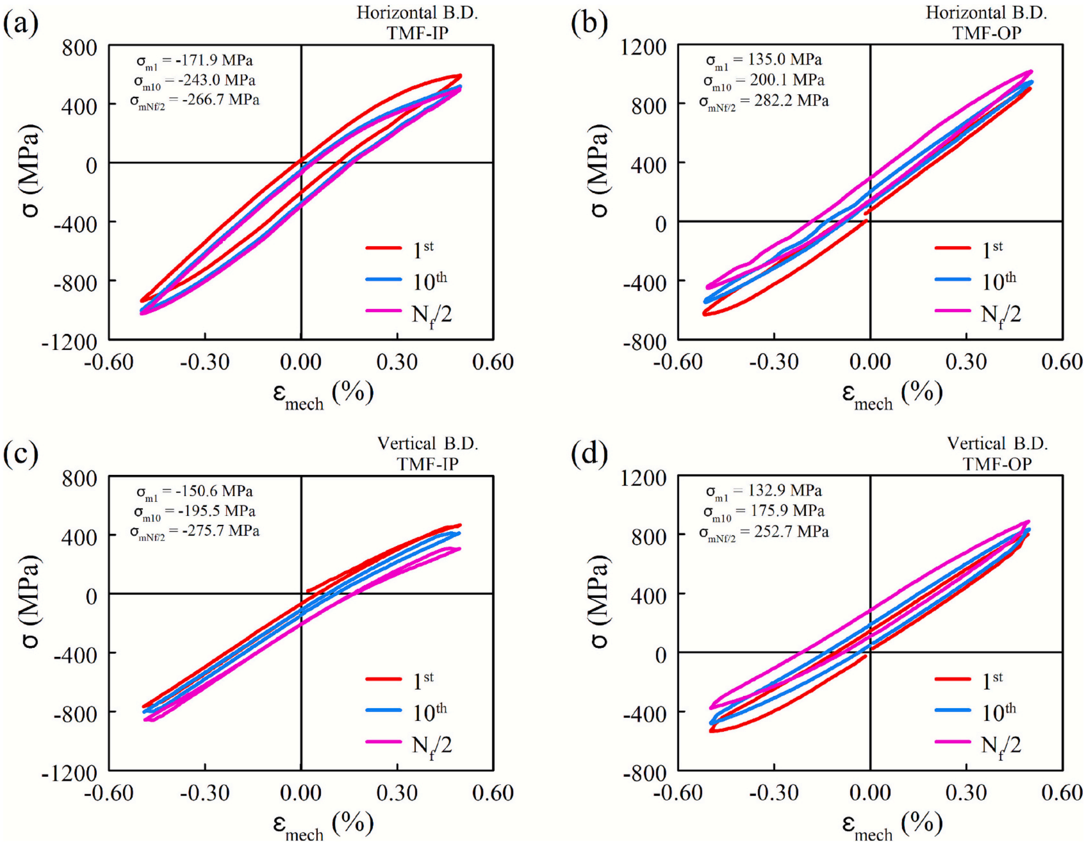

Fig. 3. Selected hysteresis loops of PBF-LB/M IN939 strained with constant mechanical strain amplitude ε_{amech} = 0.5%. (a) horizontally built specimen – TMF-IP; (b) horizontally built specimen – TMF-OP; (c) vertically built specimen – TMF-IP; (d) horizontally built specimen – TMF-OP.

Table 2
Results of TMF experiments.

		ε_{amech} (%)	σ_a (MPa)	ε_{ap} (%)	N_f
Horizontal B.D.	TMF-IP	0.30	561.7	0.00998	10,000
		0.40	652.3	0.01163	1155
		0.45	730.7	0.02361	295
		0.50	754.3	0.06191	35
	TMF-OP	0.30	498.8	0.00113	4740
		0.35	559.4	0.00141	2667
		0.40	628.6	0.00950	1875
		0.50	734.2	0.04870	863
		0.60	831.1	0.00080	270
Vertical B.D.	TMF-IP	0.40	452.9	0.00293	6686
		0.45	498.8	0.00569	7076
		0.50	584.7	0.01591	1454
		0.60	619.6	0.04879	350
		0.70	708.9	0.09968	86
	TMF-OP	0.40	530.4	0.03315	3661
		0.50	629.7	0.06422	1852
		0.60	693.1	0.09902	841
		0.70	754.3	0.15404	686
		0.90	878.3	0.24971	240

perpendicular to B.D. subjected to TMF-IP and TMF-OP loading, respectively, whereas Fig. 4c and Fig. 4d show the stress development for vertically printed samples with the loading axis parallel to the B.D. The curves emphasise what has already been said earlier in the case of hysteresis loops, namely that compressive mean stress develops in the case of TMF-IP loading and tensile mean stress in the case of TMF-OP loading. This is typical across the entire range of selected mechanical strain amplitudes. Mild cyclic softening was observed in all TMF tests, regardless of the B.D., applied strain amplitude, and the phase shift between temperature and mechanical strain.

The cyclic stress–strain curves (CSSCs) obtained under TMF-IP and TMF-OP testing conditions are presented in Fig. 5. The CSSCs were evaluated for specimens produced in both horizontal and vertical build orientations, illustrating the relationship between stress amplitude (σ_a) and plastic strain amplitude (ε_{ap}) assessed from the recorded hysteresis loops at half of the fatigue lifetime. An evident influence of build orientation on the cyclic stress–strain response is observed. The horizontally built specimens consistently exhibit higher stress amplitudes at a given plastic strain amplitude compared to their vertically built counterparts. The differences in cyclic response between orientations are apparent under both TMF-IP and TMF-OP conditions. Under TMF-OP conditions, this difference diminishes with increasing strain amplitude, while an opposite trend is evident under TMF-IP conditions.

3.3. *TMF lifetime*

The fatigue lifetime results of PBF-LB/M IN939 under TMF conditions are summarised in Fig. 6, where the mechanical strain amplitude (ε_{amech}) is plotted as a function of the number of cycles to failure (N_f) on a semi-logarithmic scale. The diagram includes data for both TMF-IP and TMF-OP loading scenarios, comparing specimens produced in horizontal and vertical build orientations. As expected for nickel-based superalloys subjected to TMF loading, TMF-IP yields generally shorter lifetimes than TMF-OP, particularly in the higher mechanical strain amplitude domain. However, as the mechanical strain amplitude decreases, crossing occurs, suggesting a change in the degradation mechanism from fatigue-creep-dominated to fatigue-oxidation-dominated [24,38,39]. Focusing on the building orientation, the vertically built IN939 maintains a life advantage over the horizontally built IN939 in TMF loading conditions, underscoring the dominant role of microstructural anisotropy.

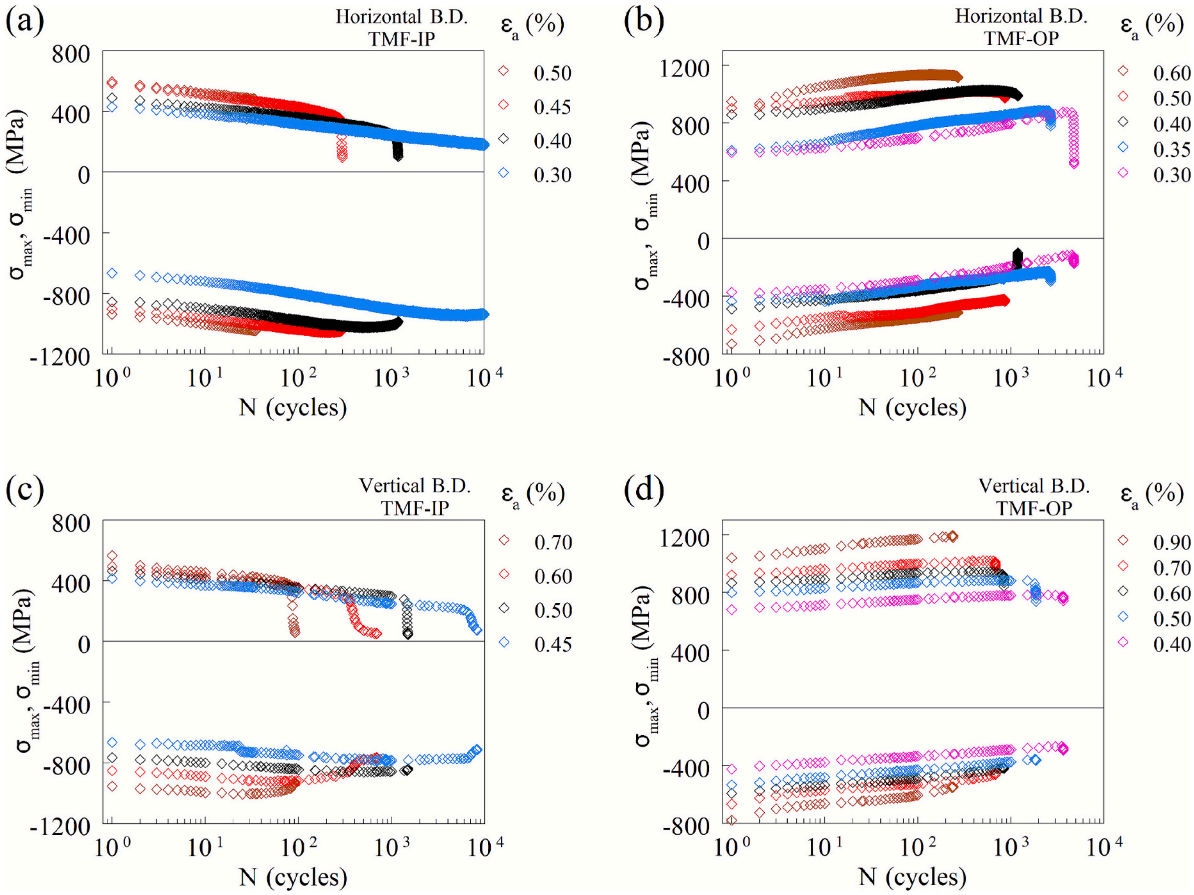

Fig. 4. Evolution of maximum and minimum stress during TMF loading of PBF-LB/M IN939. (a) horizontally built specimens – TMF-IP; (b) horizontally built specimens – TMF-OP; (c) vertically built specimens – TMF-IP; (d) horizontally built specimens – TMF-OP.

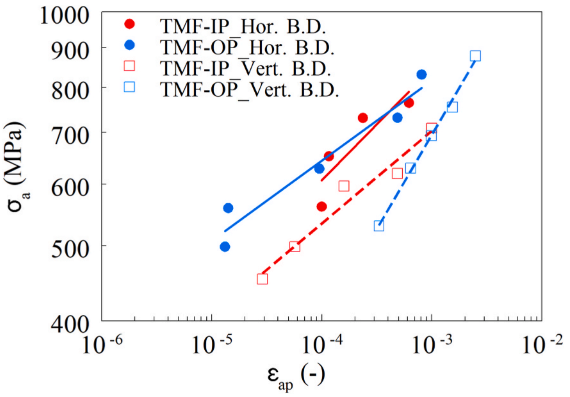

Fig. 5. Cyclic stress–strain curves of PBF-LB/M IN939 subjected to TMF loading in the temperature range of 400-800 °C.

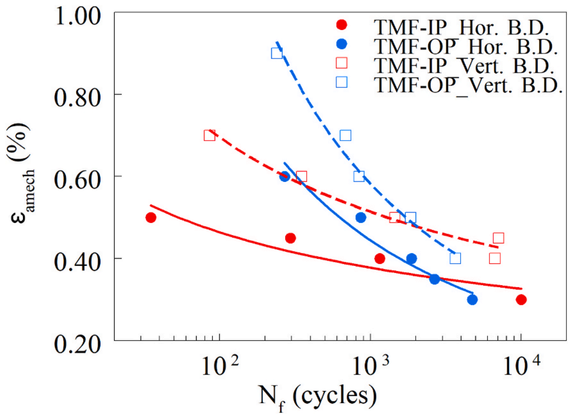

Fig. 6. Effect of B.D. and phase shift on TMF lifetime of PBF-LB/M IN939.

3.4. Microstructural degradation

Fig. 7 and Fig. 8 compile longitudinal SEM micrographs and EBSD maps, respectively, of PBF-LB/M IN939 after TMF, highlighting characteristic fatigue damage for both horizontally and vertically built specimens. Long internal grain-boundary cracks perpendicular to the loading axis were found in both horizontally and vertically built specimens after TMF-IP loading (Fig. 7a and Fig. 7c). Contrary to this, relatively short cracks parallel to the loading direction were found under TMF-OP conditions for vertically built material (Fig. 7d), suggesting grain boundary sliding [40]. Interestingly, nothing comparable was observed in horizontally oriented material under TMF-OP loading, where cavities appeared only exceptionally at the junctions of several grains (Fig. 7b).

During TMF-IP cycling, crack paths are dominantly intergranular along grain boundaries (Fig. 8a and Fig. 8c), and the cracks appear winding. Many cracks are subsurface and do not break through to the exterior (Fig. 7), which is true especially in the case of vertically built material, where internal intergranular damage dominates and surface cracks are very shallow (Fig. 7c). Once the grain boundaries are oriented perpendicular to the loading axis, i.e., horizontally built material, the grain boundary cracks connect easily to the surface, as shown in Fig. 8a.

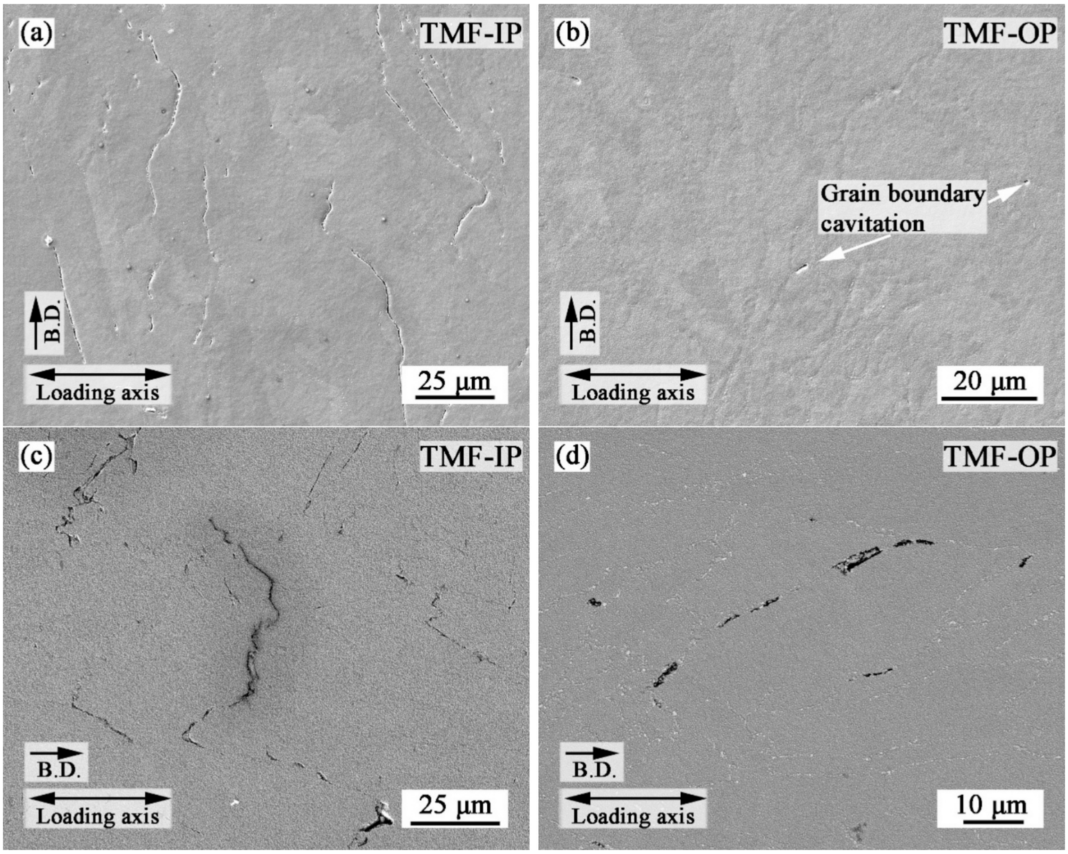

Fig. 7. SEM micrographs of internal damage due to TMF loading of PBF-LB/M IN939. (a) horizontal B.D. – TMF-IP, $\varepsilon_{amech} = 0.4\%$ and $N_f = 1155$ cycles; (b) horizontal B.D. – TMF-OP, $\varepsilon_{amech} = 0.5\%$ and $N_f = 863$ cycles; (c) vertical B.D. – TMF-IP, $\varepsilon_{amech} = 0.7\%$ and $N_f = 86$ cycles; (d) vertical B.D. – TMF-OP, $\varepsilon_{amech} = 0.9\%$ and $N_f = 240$ cycles.

In contrast, TMF-OP cycling tends to produce sharp, surface-initiated cracks that propagate transgranularly, mainly perpendicular to the loading axis (Fig. 8d). However, due to the very frequent presence of grain boundaries, cracks in horizontally built IN939 tend to propagate along grain boundaries as well, when convenient (Fig. 8b).

Representative micrographs of the post-TMF dislocation arrangements for each loading mode are presented in Fig. 9. A common feature, regardless of the B.D. and the type of TMF loading cycle, is the presence of stacking faults in coarse $\acute{\gamma}$ precipitates. Nevertheless, their occurrence is significantly more frequent under TMF-IP loading (Fig. 9a and Fig. 9e). A typical feature associated with TMF-IP loading is the formation of a zig-zag dislocation network, as shown in detail in Fig. 9b, which is characteristic of creep deformation [41,42]. In the case of a horizontally built PBF–LB/M IN939 superalloy, twin formation was observed regularly under TMF-IP loading conditions (Fig. 9a) and only rarely under TMF-OP loading conditions (Fig. 9d). In contrast, no twins were observed for the vertical B.D. TMF-OP loading produced typically planar dislocation arrays (persistent slip bands – PSBs) parallel to octahedral slip planes. PSBs cut through both $\acute{\gamma}$ precipitates and γ matrix. As evident from Fig. 9c and Fig. 9f, even dislocation-rich cell walls pose no obstacle to PSBs [20].

4. Discussion

4.1. *Effect of the phase angle on TMF lifetime*

The TMF results on PBF–LB/M IN939 can be rationalised in a creep–fatigue interaction framework in the spirit of Taira's model [43], whose life-fraction concept for TMF loading was thoroughly reviewed in [44]. In this view, failure ensues when the time–dependent creep damage accumulated during the high–temperature portions of the fatigue cycle and the time–independent cyclic fatigue damage together reach a critical life fraction, i.e. a Robinson–Taira–type summation in which the creep contribution is weighted by the actual stress–temperature history and the fatigue contribution depends primarily on the plastic strain range and peak stresses reached during cycling [24,45,46]. In our experiments, the phase relation determines when high stress coincides with high temperature, thereby setting the relative share of creep and fatigue damage per cycle. Specifically, TMF-IP cycles place the tensile half–cycle at the maximum temperature, allowing creep relaxation to occur during the tensile segment, thereby promoting grain–boundary (GB) sliding. Conversely, the TMF-OP cycle places compression at the maximum temperature and tension at the minimum temperature, so cyclic/oxidation mechanisms dominate TMF damage, while creep under compression relaxes stresses (Figs. 3–4). The observed intergranular, often subsurface, cracks in TMF-IP and sharper, largely transgranular surface-connected cracks in TMF-OP (Figs. 7–8) are consistent with this partitioning of mechanisms in PBF–LB/M IN939 under 400–800 °C TMF loading. The damage partitioning was also confirmed for other additively manufactured superalloys [15,47–49].

The TMF-IP/TMF-OP life curves crossover at lower strain amplitudes (Fig. 6) naturally emerges when the evolution of peak stresses is considered (Fig. 4). During TMF-IP cyclic loading, the high-temperature tensile half-cycle allows creep relaxation, so peak tensile stress decreases and a compressive mean stress develops with cycling. This progressively reduces the driving force for fatigue crack propagation even as creep damage accumulates. In TMF-OP, the high-temperature compressive half–cycle relaxes compression, but the low-temperature tension is not relaxed. Therefore, the peak tensile stress increases and a tensile mean stress advances, raising the driving force for fatigue crack initiation and

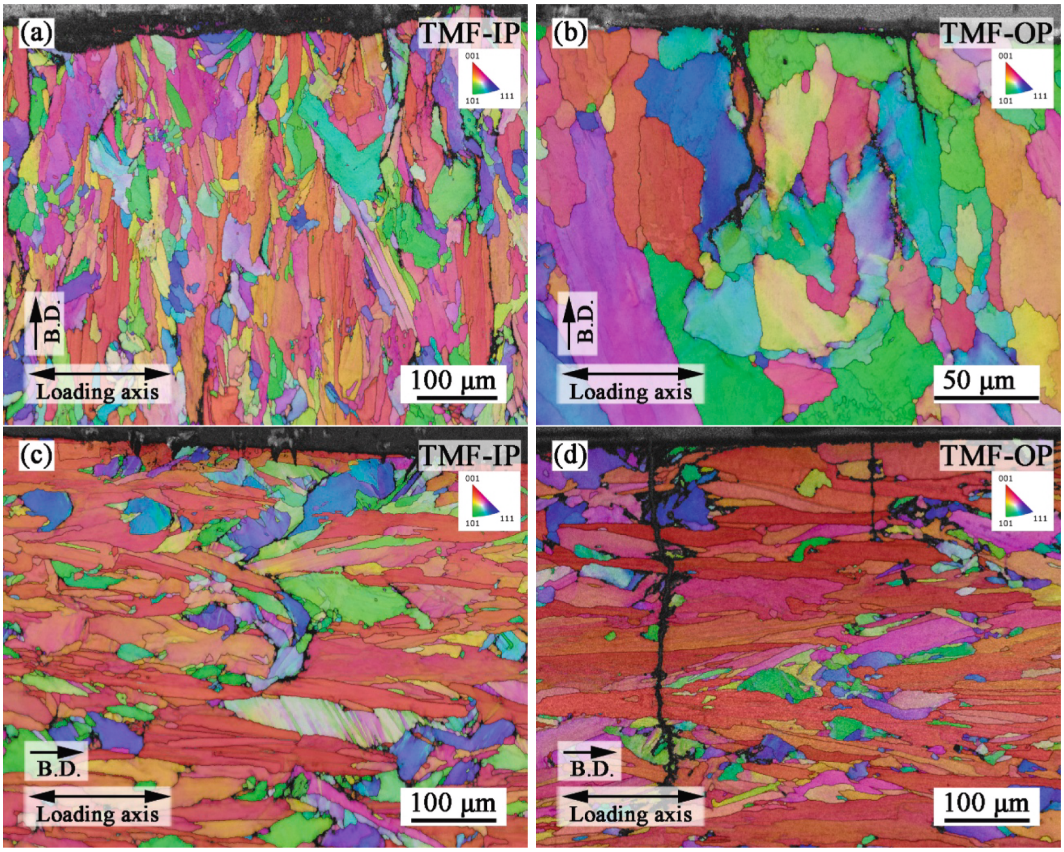

Fig. 8. EBSD mapping of fatigue crack initiation and propagation under TMF loading. (a) horizontal B.D. – TMF-IP, $\varepsilon_{amech} = 0.4\%$ and $N_f = 1155$ cycles; (b) horizontal B.D. – TMF-OP, $\varepsilon_{amech} = 0.5\%$ and $N_f = 863$ cycles; (c) vertical B.D. – TMF-IP, $\varepsilon_{amech} = 0.7\%$ and $N_f = 86$ cycles; (d) vertical B.D. – TMF-OP, $\varepsilon_{amech} = 0.7\%$ and $N_f = 686$ cycles.

subsequent propagation. At higher mechanical strain amplitudes, TMF-IP remains more damaging due to dominant creep damage (grain boundary damage – Fig. 7 and Fig. 8). As mechanical strain amplitude decreases and creep-assisted damage diminishes, the increase of peak tensile stress in TMF-OP erodes the advantage of TMF-OP cycle, producing the crossover [29]. This underscores a key practical point of this study: TMF life of IN939 is governed by the (phase-specific, orientation-dependent) stress response and its cycle-wise evolution (Figs. 4–6).

The damage observed via SEM (Fig. 7) and SEM/EBSD analysis (Fig. 8) supports the different dominant damage mechanisms under TMF-IP and TMF-OP loading. The presence of intergranular, often subsurface cracks in TMF-IP, typical for creep-dominated damage, versus sharp surface-initiated transgranular cracks perpendicular to the loading axis in TMF-OP, typical for fatigue-dominated damage, was observed. However, for both TMF-IP and TMF-OP loading, intergranular damage occurred (Fig. 7), probably as a result of grain boundary sliding. The orientation of these boundary cracks relative to the applied load can be rationalised using the framework of Taira [40,43]. In type 304 austenitic steel, they scribed intersecting fiducial lines across grain boundaries and tracked the offsets of those markers, demonstrating boundary-parallel displacement caused by sliding under both tension and compression [40]. Because sliding occurs only at elevated temperatures, it is activated by tensile stress during TMF-IP loading and by compressive stress during TMF-OP loading. Consequently, boundary cracks formed in TMF-IP loading typically intersect the load axis at large angles. In contrast, in TMF-OP loading, cracks tend to run at shallow angles to the loading direction. This trend matches the observations in Fig. 7 and has also been reported for the nickel-based NiCr22Co12Mo9 alloy [30]. The intergranular cracks, perpendicular to the loading axis (TMF-IP – Fig. 7a and 7c), typically result in shorter lifetimes (Fig. 6) due to facilitated transverse crack opening; i.e., if the crack is suitably oriented, a smaller tensile stress is sufficient for it to propagate. On the other hand, intergranular cracks parallel to the loading axis (Fig. 7d) are considered not to be as detrimental at the beginning of TMF lifetime. However, microcracks may partially open and kink/rotate toward a more transverse path to increase energy release [50], becoming potentially more damaging later in TMF life. This can eventually partially contribute to the observed crossover of fatigue life curves in Fig. 6.

4.2. *Effect of the building orientation on TMF lifetime*

A central empirical result of this study is that horizontally built (load perpendicular to B.D.) specimens sustain a higher cyclic stress response than vertically built (load parallel to B.D.) specimens at the same mechanical strain amplitude (Fig. 4 and Fig. 5), and, correspondingly, exhibit shorter TMF lives (Fig. 6). Two microstructural causes act in concert here. First, the PBF–LB/M IN939 shows a pronounced $\langle 001 \rangle$ texture along the B.D. (Fig. 2b). Cyclic straining parallel to B.D. therefore probes many grains in near $\langle 001 \rangle$ orientation, whereas loading perpendicular to B.D. engages a broader spread with rather $\langle 011 \rangle$ components (Fig. 2a). Given the elastic–plastic anisotropy of face-centred cubic nickel-based superalloys with ordered γ' precipitates, this orientation shift raises the effective modulus and kinematic constraints for horizontally built PBF–LB/M IN939. Consequently, under strain-controlled loading, horizontally printed specimens naturally develop higher stress levels. Second, the elongated columnar grains and grain boundary/cell–wall decorations (carbides, dislocation walls) are aligned with B.D. Thus, loading of horizontally built specimens intersects a higher density of transverse grain boundaries and barriers, increasing back-stress and facilitating faster crack linkage to the surface,

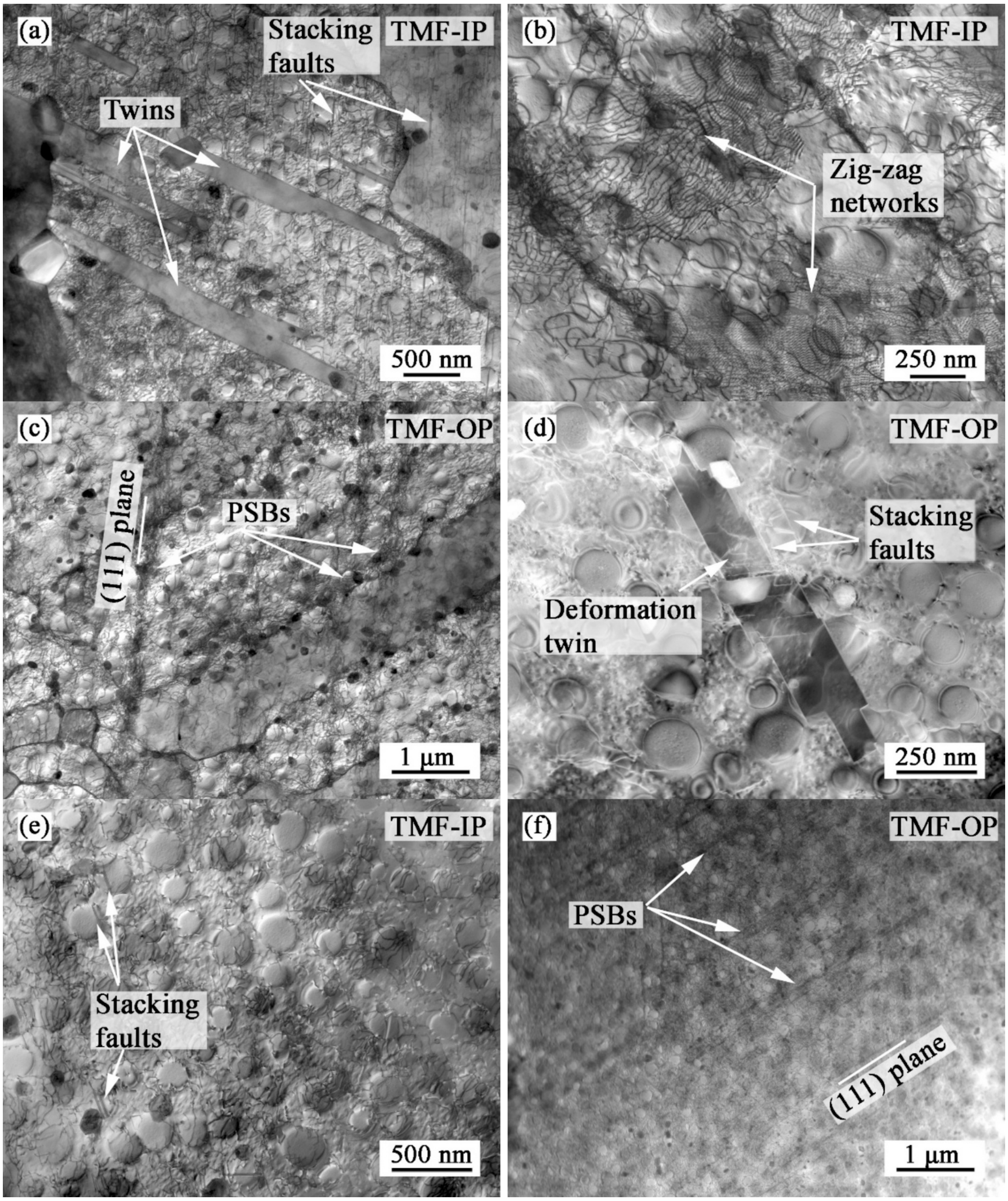

Fig. 9. BF and HAADF STEM micrographs of the internal dislocation arrangement of PBF-LB/M IN939 subjected to TMF loading. (a) horizontal B.D. – TMF-IP, $\varepsilon_{amech} = 0.5\%$ and $N_f = 35$ cycles; (b) horizontal B.D. – TMF-IP, $\varepsilon_{amech} = 0.3\%$ and $N_f = 10000$ cycles (c) horizontal B.D. – TMF-OP, $\varepsilon_{amech} = 0.4\%$ and $N_f = 1875$ cycles; (d) horizontal B.D. – TMF-OP, $\varepsilon_{amech} = 0.6\%$ and $N_f = 270$ cycles (e) vertical B.D. – TMF-IP, $\varepsilon_{amech} = 0.7\%$ and $N_f = 86$ cycles; (f) vertical B.D. – TMF-OP, $\varepsilon_{amech} = 0.7\%$ and $N_f = 686$ cycles.

especially under TMF-IP (Fig. 7 and Fig. 8). Because the Taira–type damage terms scale with stress response (fatigue via plastic strain range ($\Delta\varepsilon_p$) and creep via time to rupture (t_r)), this orientation-induced increase of stress amplitude is a proximate cause of the shorter TMF life of horizontally built specimens observed here (Fig. 5 and Fig. 6). Various fatigue studies on other superalloys, such as IN718 [15,48,51], IN939 [20,21], Hastelloy X [52], as well as stainless steels like 316 L [27,34] or 304 [53], report the same linkage between build–direction microstructure, stress response, and lifetime, supporting our findings.

4.3. Microtwinning

An interesting deformation feature is the appearance of twins exclusively in the horizontally built superalloy (Fig. 9a). This selectivity can be explained by Kolbe's model for microtwinning in γ'–strengthened nickel-based superalloys. It was demonstrated that above ~ 700–780 °C, a change in mechanism can occur. Viscous motion of $a/6\langle 112\rangle$ partials drags intrinsic stacking faults in γ' and produces microtwins; the favourable conditions include tension along $\langle 011\rangle$ or compression along $\langle 001\rangle$, which maximise the resolved shear on the twinning partials and enable thermally assisted re–ordering within γ' precipitates [54]. In our configuration, TMF-IP loading for horizontal B.D. applies tension at a maximum temperature of 800 °C to a texture that contains substantial near $\langle 110\rangle$ components relative to the load (Figs. 2a, 3a), which is precisely the Kolbe-permissive state, hence the observed twins (Fig. 9a). Under TMF-OP conditions, where the compressive half-cycle occurs at maximum temperature, twinning can still happen via two mutually reinforcing routes. Firstly, a distribution around the preferred orientations (Figs. 2a–b) does not prohibit the occurrence of grains with other orientations so that a small grain population will be loaded near the

⟨001⟩ orientation in the horizontally built specimens. Those grains can satisfy Kolbe's model, and twinning can thus occur during the high-temperature compressive segment of the TMF-OP cycle. Secondly, the microstructure after TMF-OP loading of horizontally built PBF–LB/M IN939 exhibits dense planar PSBs (Fig. 9c), which likely form during the low-temperature part of the cycle and can produce superlattice stacking faults (SSFs) in the γ' precipitates. Upon the subsequent high-temperature compressive half-cycle, these SSFs can thicken into twins through Kolbe-type re-ordering, provided the compressive peak is high enough [54–57]. Independent TMF and high-temperature compression studies on single-crystal superalloys corroborate that TMF-OP loading can localise microtwin plates during the compressive half-cycle near crack tips, and that compression at high-temperature in near ⟨001⟩ crystals promotes microtwinning once the threshold stress is exceeded [55,56]. Put differently, TMF-OP loading of horizontally built PBF–LB/M IN939 has the right combination of high compressive peaks at maximum temperature due to its intrinsically higher stress response (Fig. 3 and Fig. 4) and crystal-to-crystal orientation spread (Fig. 2), to activate the Kolbe mechanism in a subset of grains even though the texture is biased toward ⟨110⟩. In the case of vertically built specimens, TMF-OP loading applies compression at maximum temperature to near ⟨001⟩ grains (Fig. 2), a combination that can also favour twinning according to the model. However, no unambiguous twins were found in our vertically built specimens under TMF-OP loading. Their absence can be attributed to several factors. Insufficient compressive peak stress (Fig. 3 and Fig. 4) or time at peak to surmount the twinning threshold in the PBF–LB/M IN939 superalloy. There can also be a competition from grain boundary-mediated relaxation (sliding/cavitation) during the high-temperature compressive segment of the TMF cycle, which reduces the local shear stress required for twin thickening. Here, it must be taken into account that TEM analysis is very local, and given the size of the deformation twins observed in horizontally built samples (Fig. 9a and Fig. 9c), it cannot be completely ruled out that deformation twinning will not happen under TMF-OP loading for vertically built PBF–LB/M IN939 superalloy.

5. Conclusions

This study systematically mapped the thermomechanical fatigue TMF behaviour of precipitation–hardened, PBF–LB/M Inconel 939 between 400 and 800 °C under in-phase (TMF–IP) and out-of-phase (TMF–OP) strain-controlled loading for vertically and horizontally built specimens. The following conclusions can be drawn from the obtained results.

1) The building direction controls the stress response and fatigue life. At a given plastic strain amplitude, horizontally built specimens developed higher stress amplitudes than vertically built specimens and consistently exhibited shorter TMF lives. This stems from the pronounced ⟨001⟩ texture and elongated columnar grains, which are aligned with the building direction.
2) Phase shift between temperature and strain sets the damage partitioning and produces a life-curve crossover. TMF-IP generated compressive mean stresses, TMF-OP generated tensile mean stresses. TMF-IP was more damaging at higher mechanical strain amplitudes. However, as the mechanical strain amplitude decreased, the TMF-IP and TMF-OP life curves crossed, consistent with a shift from creep-assisted fatigue damage coupled with grain-boundary degradation toward fatigue-dominated mechanisms that are promoted by the rising tensile mean stress in TMF-OP.
3) TMF-IP produced predominantly intergranular, often subsurface cracks, whereas TMF-OP promoted sharp, surface-initiated cracks with largely transgranular propagation; grain-boundary-parallel microcracks consistent with boundary sliding were additionally observed in vertically built material under TMF-OP.
4) Slightly different deformation mechanisms reflect the phase-dependent loading path and preferential texture orientation. TMF-IP produced zig-zag dislocation networks indicative of a creep deformation mechanism. TMF-OP loading was characterised by dense planar persistent slip bands that cut through the γ matrix and $\acute{\gamma}$ precipitates, with dislocation-rich cell walls offering little resistance. Both TMF-IP and TMF-OP exhibited stacking faults within the γ' precipitates, regardless of building direction.
5) TMF loading produced microtwins exclusively in horizontally built specimens, with twinning most pronounced under TMF-IP and only sporadically observed under TMF-OP, reflecting favourable grain orientations and the higher cyclic stresses needed to activate Kolbe-type twinning.

Overall, the results provide an orientation-aware TMF dataset and mechanistic framework for PBF–LB/M IN939 connecting texture and grain morphology to phase-dependent stress responses, cracking modes, and lifetime. These insights enable more reliable TMF lifetime assessments and microstructure-informed design choices for additively manufactured hot-section components.

CRediT authorship contribution statement

Ivo Šulák: Writing – review & editing, Writing – original draft, Visualization, Supervision, Project administration, Investigation, Formal analysis, Data curation, Conceptualization. **Markéta Gálíková:** Visualization, Methodology, Investigation, Formal analysis, Data curation. **Tomáš Babinský:** Writing – review & editing, Visualization, Methodology, Formal analysis. **Ladislav Poczklán:** Writing – review & editing, Methodology, Investigation, Formal analysis. **Ivo Kuběna:** Writing – review & editing, Validation, Supervision, Project administration, Funding acquisition, Formal analysis, Conceptualization. **Stefan Guth:** Writing – review & editing, Writing – original draft, Supervision, Investigation, Data curation, Conceptualization.

Declaration of competing interest

The authors declare that they have no known competing financial interests or personal relationships that could have appeared to influence the work reported in this paper.

Acknowledgements

The present research was financially supported by the grant No. 23-06167S of the Czech Science Foundation (GACR). Ivo Šulák and Ladislav Poczklán acknowledge the support of the Czech Academy of Sciences under the framework of the Lumina quaeruntur project. Ivo Kuběna appreciates the support from the Czech Academy of Sciences Strategy AV21 scheme as part of „The power of objects: Materiality between past and future“ grant at the Institute of Physics of Materials. This publication was supported by the project “Mechanical Engineering of Biological and Bio-inspired Systems”, funded as project No. CZ.02.01.01/00/22_008/0004634 by Programme Johannes Amos Comenius, call Excellent Research.

Data availability

The original data in this work are available from 10.5281/zenodo.17659067

References

[1] Kanagarajah P, Brenne F, Niendorf T, Maier HJ. Inconel 939 processed by selective laser melting: Effect of microstructure and temperature on the mechanical properties under static and cyclic loading. Mater Sci Eng A 2013;588:188–95. https://doi.org/10.1016/j.msea.2013.09.025.

[2] Banoth S, Li C-W, Hiratsuka Y, Kakehi K. The effect of recrystallization on creep properties of alloy IN939 fabricated by selective laser melting process. Metals 2020;10:1016. https://doi.org/10.3390/met10081016.
[3] Doğu MN, Ozer S, Yalçın MA, Davut K, Bilgin GM, Obeidi MA, et al. Effect of solution heat treatment on the microstructure and crystallographic texture of IN939 fabricated by powder bed fusion-laser beam. J Mater Res Technol 2023;24:8909–23. https://doi.org/10.1016/j.jmrt.2023.05.152.
[4] Rodríguez-Barber I, Fernández-Blanco AM, Unanue-Arruti I, Madariaga-Rodríguez I, Milenkovic S, Pérez-Prado MT. Laser powder bed fusion of the Ni superalloy Inconel 939 using pulsed wave emission. Mater Sci Eng A 2023;870:144864. https://doi.org/10.1016/j.msea.2023.144864.
[5] Šulák I, Babinský T, Chlupová A, Milovanović A, Náhlík L. Effect of building direction and heat treatment on mechanical properties of Inconel 939 prepared by additive manufacturing. J Mech Sci Technol 2023;37:1071–6. https://doi.org/10.1007/s12206-022-2101-7.
[6] Raza SA, Canyurt OE, Sezer HK. A systematic review of Inconel 939 alloy parts development via additive manufacturing process. Heliyon 2024;10:e25506. https://doi.org/10.1016/j.heliyon.2024.e25506.
[7] Hu P, Liu Z, Zhang H, Li Y, Zhou Q, Xie J. Effect of remelting on cracking of Inconel 939 fabricated via laser powder bed fusion. Mater Charact 2024;214:114087. https://doi.org/10.1016/j.matchar.2024.114087.
[8] Ozer S, Doğu MN, Ozdemirel C, Bilgin GM, Gunes M, Davut K, et al. Effect of aging treatment on the microstructure, cracking type and crystallographic texture of IN939 fabricated by powder bed fusion-laser beam. J Mater Res Technol 2024;33:574–88. https://doi.org/10.1016/j.jmrt.2024.09.106.
[9] Shahwaz M, Nath P, Sen I. Recent advances in additive manufacturing technologies for Ni-based Inconel superalloys – A comprehensive review. J Alloy Compd 2025;1010:177654. https://doi.org/10.1016/j.jallcom.2024.177654.
[10] Sedlak J, Zouhar J, Pokorny Z, Robl J, Kolomy S, Pagac M, et al. Effect of heat treatment and hot isostatic pressing on the structure and mechanical properties of Inconel 939 manufactured via casting and LPBF. J Manuf Process 2025;145:556–70. https://doi.org/10.1016/j.jmapro.2025.04.082.
[11] Mostafaei A, Ghiaasiaan R, Ho I-T, Strayer S, Chang K-C, Shamsaei N, et al. Additive manufacturing of nickel-based superalloys: A state-of-the-art review on process-structure-defect-property relationship. Prog Mater Sci 2023;136:101108. https://doi.org/10.1016/j.pmatsci.2023.101108.
[12] Tang YT, Panwisawas C, Ghoussoub JN, Gong Y, Clark JWG, Németh AAN, et al. Alloys-by-design: Application to new superalloys for additive manufacturing. Acta Mater 2021;202:417–36. https://doi.org/10.1016/j.actamat.2020.09.023.
[13] Marchese G, Parizia S, Saboori A, Manfredi D, Lombardi M, Fino P, et al. The influence of the process parameters on the densification and microstructure development of laser powder bed fused inconel 939. Metals 2020;10:882. https://doi.org/10.3390/met10070882.
[14] Gokcekaya O, Ishimoto T, Hibino S, Yasutomi J, Narushima T, Nakano T. Unique crystallographic texture formation in Inconel 718 by laser powder bed fusion and its effect on mechanical anisotropy. Acta Mater 2021;212:116876. https://doi.org/10.1016/j.actamat.2021.116876.
[15] Guth S, Babinský T, Antusch S, Klein A, Kuntz D, Šulák I. Creep–fatigue interaction of Inconel 718 manufactured by electron beam melting. Adv Eng Mater 2023:2300294. https://doi.org/10.1002/adem.202300294.
[16] Li S, Gao S, Zhang W, Lu G, Cui L, Li L, et al. Study of the crack and porosity regulation of a non-weldable Ni-based superalloy fabricated by laser powder bed fusion. J Mater Eng Perform 2025;34:15854–65. https://doi.org/10.1007/s11665-024-10362-4.
[17] Zeng C, Ding H, Bhandari U, Guo SM. Design of crack-free laser additive manufactured Inconel 939 alloy driven by computational thermodynamics method. MRS Commun 2022;12:844–9. https://doi.org/10.1557/s43579-022-00253-x.
[18] Zhang B, Ding H, Meng AC, Nemati S, Guo S, Meng WJ. Crack reduction in Inconel 939 with Si addition processed by laser powder bed fusion additive manufacturing. Addit Manuf 2023;72:103623. https://doi.org/10.1016/j.addma.2023.103623.
[19] Bae J-S, Tekoglu E, Alrizqi M, O'Brien AD, Liu J, Biggs K, et al. Additive manufacturing of strong and ductile In939+TiB2 by laser powder bed fusion. Mater Sci Eng A 2025;939:148446. https://doi.org/10.1016/j.msea.2025.148446.
[20] Babinský T, Šulák I, Gálíková M, Kuběna I, Poloprudský J, Náhlík L. Room-temperature low-cycle fatigue behaviour of cast and additively manufactured IN939 superalloy. Mater Sci Eng A 2025;924:147730. https://doi.org/10.1016/j.msea.2024.147730.
[21] Kuběna I, Babinský T, Náhlík L, Šulák I. Cyclic stress–strain behavior of additively manufactured gamma prime strengthened superalloy at elevated temperatures. Theor Appl Fract Mech 2024;133:104623. https://doi.org/10.1016/j.tafmec.2024.104623.
[22] Šulák I, Obrtlík K. Thermomechanical and isothermal fatigue properties of MAR-M247 superalloy. Theor Appl Fract Mech 2024;131:104443. https://doi.org/10.1016/j.tafmec.2024.104443.
[23] Deng W, Xu J, Hu Y, Huang Z, Jiang L. Isothermal and thermomechanical fatigue behavior of Inconel 718 superalloy. Mater Sci Eng A 2019;742:813–9. https://doi.org/10.1016/j.msea.2018.11.052.
[24] Christ H-J, Jung A, Maier HJ, Teteruk R. Thermomechanical fatigue—damage mechanisms and mechanism-based life prediction methods. Sadhana 2003;28:147–65. https://doi.org/10.1007/BF02717131.
[25] Lancaster RJ, Whittaker MT, Williams SJ. A review of thermo-mechanical fatigue behaviour in polycrystalline nickel superalloys for turbine disc applications. Mater High Temp 2013;30:2–12. https://doi.org/10.3184/096034013X13630238172260.
[26] Zhang P, Zhu Q, Chen G, Wang C. Review on thermo-mechanical fatigue behavior of nickel-base superalloys. Mater Trans 2015;56:1930–9. https://doi.org/10.2320/matertrans.M2015323.
[27] Babinský T, Šulák I, Kuběna I, Man J, Weiser A, Švábenská E, et al. Thermomechanical fatigue of additively manufactured 316L stainless steel. Mater Sci Eng A 2023;869:144831. https://doi.org/10.1016/j.msea.2023.144831.
[28] Moverare J, Lancaster RJ, Jones J, Stekovic S, Whittaker MT. A review of recent advances in the understanding of thermomechanical fatigue durability and failure mechanisms in nickel-based superalloys. Metall Mater Trans A 2025;56:1115–34. https://doi.org/10.1007/s11661-025-07698-4.
[29] Guth S, Doll S, Lang K-H. Influence of phase angle on lifetime, cyclic deformation and damage behavior of Mar-M247 LC under thermo-mechanical fatigue. Mater Sci Eng A 2015;642:42–8. https://doi.org/10.1016/j.msea.2015.06.055.
[30] Guth S, Lang K-H. An approach to lifetime prediction for a wrought Ni-base alloy under thermo-mechanical fatigue with various phase angles between temperature and mechanical strain. Int J Fatigue 2017;99:286–94. https://doi.org/10.1016/j.ijfatigue.2016.10.015.
[31] Petráš R, Šulák I, Polák J. The effect of dwell on thermomechanical fatigue in superaustenitic steel Sanicro 25. Fatigue Fract Eng Mater Struct 2021;44:673–88. https://doi.org/10.1111/ffe.13385.
[32] De Luca DM, Hamilton AR, Reed PAS. Influence of build orientation on high temperature fatigue crack growth mechanisms in Inconel 718 fabricated by laser powder bed fusion: Effects of temperature and hold time. Int J Fatigue 2023;170:107484. https://doi.org/10.1016/j.ijfatigue.2022.107484.
[33] Rashkovets M, Kislov N, Gushchina M, Nikulina A, Popelukh A, Klimova-Korsmik O. Phase composition and fatigue crack growth behavior of Inconel 718 under additive manufacturing. Mater Sci Eng A 2022;851:143595. https://doi.org/10.1016/j.msea.2022.143595.
[34] Babinský T, Šulák I, Poczklán L, Guth S. A comparison of conventional and additively manufactured 316L under thermomechanical fatigue. Int J Fatigue 2024;187:108477. https://doi.org/10.1016/j.ijfatigue.2024.108477.
[35] Sadeghi E, Karimi P, Esmaeilizadeh R, Berto F, Shao S, Moverare J, et al. A state-of-the-art review on fatigue performance of powder bed fusion-built alloy 718. Prog Mater Sci 2023;133:101066. https://doi.org/10.1016/j.pmatsci.2022.101066.
[36] Šulák I, Hrbáček K, Obrtlík K. The effect of temperature and phase shift on the thermomechanical fatigue of nickel-based superalloy. Metals 2022;12:993. https://doi.org/10.3390/met12060993.
[37] Hähner P. Validated code-of-practice for strain-controlled thermo-mechanical fatigue testing. Luxembourg: Office for Official Publications of the European Communities; 2006.
[38] Neu RW, Sehitoglu H. Thermomechanical fatigue, oxidation, and creep: Part i. Damage mechanisms. Metall Trans A 1989;20:1755–67. https://doi.org/10.1007/BF02663207.
[39] Šulák I, Obrtlík K. The effect of dwell on thermomechanical fatigue behaviour of Ni-base superalloy Inconel 713LC. Int J Fatigue 2023;166:107238. https://doi.org/10.1016/j.ijfatigue.2022.107238.
[40] Fujino M, Taira S. Effectof thermal cycle on low cycle fatigue life of steels and grain boundary sliding characteristics. Mech Behav Mater, Elsevier 1980:49–58. https://doi.org/10.1016/B978-1-4832-8414-9.50030-4.
[41] Sirrenberg M, Babinský T, Bürger D, Guth S, Parsa AB, Thome P, et al. The high temperature strength of single crystal ni-base superalloys – Re-visiting constant strain rate, creep, and thermomechanical fatigue testing. Adv Eng Mater 2024;26:2400368. https://doi.org/10.1002/adem.202400368.
[42] Tao X, Wang X, Li J, Sun X, Zhou Y. Abnormal densification of dislocation networks during creep deformation in a single crystal superalloy with a small γ/γ' lattice misfit. Scr Mater 2025;255:116399. https://doi.org/10.1016/j.scriptamat.2024.116399.
[43] Taira S, Fujino M. A damage analysis in high temperature thermal fatigue. Trans Iron Steel Inst Jpn 1979;19:185–90. https://doi.org/10.2355/isijinternational1966.19.185.
[44] Zhuang WZ, Swansson NS. Thermo-mechanical fatigue life prediction: A. Crit Rev 1988. https://scispace.com/pdf/thermo-mechanical-fatigue-life-prediction-a-critical-review-5dxqc9ft3x.pdf.
[45] M. Fujino, S. Taira, Effect of thermal cycle on low cycle fatigue life of steels and grain boundary sliding characteristics, In: Proceedings of ICM3, vol. 2, Cambridge: Pergamon Press 1979: pp. 49–58.
[46] D.A. Spera, The calculation of elevated temperature cyclic life considering low cycle fatigue and creep, (1969). https://ntrs.nasa.gov/search.jsp?R=19690020294.
[47] Zou CL, Pang JC, Li WB, Wang N, Feng YY, Li SX, et al. Thermo-mechanical fatigue behavior and life prediction of selective laser melted inconel 718. Mater Sci Eng A 2025;919:147502. https://doi.org/10.1016/j.msea.2024.147502.
[48] Guth S, Babinský T, Antusch S, Klein A, Kuntz D, Šulák I. Comparison of electron-beam-melted and conventionally rolled Inconel 718 under thermomechanical creep-fatigue loading. Int J Fatigue 2026;202:109238. https://doi.org/10.1016/j.ijfatigue.2025.109238.
[49] Zhang L, Lu L, Wang Y, Li W, Yu Z, Luo X, et al. Thermo-mechanical fatigue behaviour of an additively manufactured nickel-based superalloy: Experiments and crystal plasticity modeling. J Mater Res Technol 2025;37:4782–99. https://doi.org/10.1016/j.jmrt.2025.07.138.
[50] Cotterell B, Rice JR. Slightly curved or kinked cracks. Int J Fract 1980;16:155–69. https://doi.org/10.1007/BF00012619.
[51] Hosseini E, Popovich VA. A review of mechanical properties of additively manufactured Inconel 718. Addit Manuf 2019;30:100877. https://doi.org/10.1016/j.addma.2019.100877.

[52] Lindström T, Calmunger M, Eriksson R, Leidermark D. Fatigue behaviour of an additively manufactured ductile gas turbine superalloy. Theor Appl Fract Mech 2020;108:102604. https://doi.org/10.1016/j.tafmec.2020.102604.

[53] Šmíd M, Koutný D, Neumannová K, Chlup Z, Náhlík L, Jambor M. Cyclic behaviour and microstructural evolution of metastable austenitic stainless steel 304L produced by laser powder bed fusion. Addit Manuf 2023;68:103503. https://doi.org/10.1016/j.addma.2023.103503.

[54] Kolbe M. The high temperature decrease of the critical resolved shear stress in nickel-base superalloys. Mater Sci Eng A 2001;319–321:383–7. https://doi.org/10.1016/S0921-5093(01)00944-3.

[55] Hong HU, Yoon JG, Choi BG, Kim IS, Yoo YS, Jo CY. Localized microtwin formation and failure during out-of-phase thermomechanical fatigue of a single crystal nickel-based superalloy. Int J Fatigue 2014;69:22–7. https://doi.org/10.1016/j.ijfatigue.2013.01.015.

[56] Sun F, Zhang J, Harada H. Deformation twinning and twinning-related fracture in nickel-base single-crystal superalloys during thermomechanical fatigue cycling. Acta Mater 2014;67:45–57. https://doi.org/10.1016/j.actamat.2013.12.011.

[57] Kovarik L, Unocic RR, Li J, Sarosi P, Shen C, Wang Y, et al. Microtwinning and other shearing mechanisms at intermediate temperatures in Ni-based superalloys. Prog Mater Sci 2009;54:839–73. https://doi.org/10.1016/j.pmatsci.2009.03.010.